ACS APPLIED MATERIALS & INTERFACES

www.acsami.org Research Article

Probing Structural Variants of Irregular DNA G-Tracts ($N \leq 2$) Using MspA Nanopores

Jiadun Liu,[‡] Luoan Xiong,[‡] Yuhang Hu,[‡] Zhuofei Wang, Jing Dai, Tie Li, Xinrong Guo, Ronghui Liu,* Zhongbo Yu, Yao Li,* and Yi Li*

Cite This: https://doi.org/10.1021/acsami.4c19806 Read Online

ABSTRACT: Guanine-rich DNA sequences with short G-tracts ($n \leq 2$) are highly prevalent and abundant in the human genome, some of which are found to be associated with diseases (Maity et al.et al. *Nucleic Acids Res.* **2020**, *48* (6), 3315−3327). Unlike conventional G-quadruplexes with three or more folded layers, these sequences with G2 tracts featuring two bilayered blocks remain largely unexplored. Here, we employed nanopore experiments and all-atom molecular dynamics simulations to investigate the unwinding strengths and dynamics of these bilayered blocks. Our results demonstrated that in an electric field, the tumor-targeting element AS1411, along with its derivatives AT11 and Z-G4, strongly interacted with the M2-MspA nanopore, resulting in at least two distinct populations (types I and II events) characterized by different current blockage fractions and dwell times. Despite AS1411 being well characterized with up to eight secondary structures by nuclear magnetic resonance spectroscopy, our nanopore experiments revealed only two populations. This could be reasonably explained by (i) reversible docking with high rigidity and (ii) strand separation and translocation. Notably, a new event type (type III) for Z-G4 suggested reduced susceptibility in the last layer, contributing to its increased rigidity. Furthermore, voltage-dependent dynamics revealed that Z-G4 exhibited extended dwell times for docking and partial unwinding, unlike AT11. Our in-solution nanopore experiments and MD simulation results would benefit toward understanding the folding principles of complicated structural variants by sequences consisting of multiple short G-tracts, paving the way for the rapid identification of similar-sequence nucleic acid aptamers in molecular diagnostics and targeted therapies.

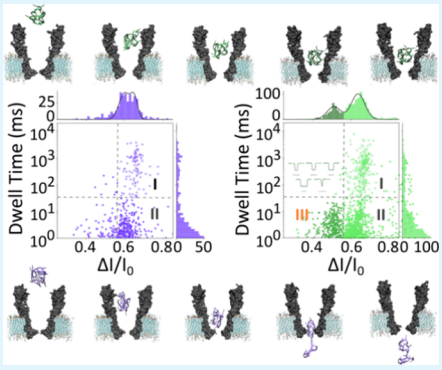

KEYWORDS: *nanopore sensing, Mycobacterium smegmatis porin A (MspA), single-molecule detection, short G-tracts, AS1411*

INTRODUCTION

G-rich DNA sequences readily form complex nucleic acid structures in which four guanine bases align in a planar arrangement and stack together to form a three-dimensional G-quadruplex (GQ) structure. Owing to their potential roles in gene regulation,[1] telomere maintenance,[2] and cancer therapy,[3] such cube-like structures have been of great interest over the past three decades. AS1411, a widely studied G-quadruplex-forming synthetic DNA oligonucleotide aptamer,[4] is known for its nuclease-resistant structure and high affinity for nucleolin (NCL), enabling it to effectively inhibit the proliferation of various tumor cell lines.[4] Researchers have also engineered AS1411-based aptamer-nanomaterial conjugates to specifically target nucleolin, which is overexpressed on cancer cell surfaces.[5,6] These nanomaterials are designed to deliver drugs that suppress human telomerase reverse transcriptase (hTERT) expression, effectively reducing hTERT levels, disrupting telomerase function, and exerting anticancer effects.[5,6] The folding quality of individual AS1411 in physiological environments is key for these applications. However, the relationship between the structure of AS1411 and its biological activities remains an open question.

Identifying the biologically relevant structure(s) of AS1411 is a significant challenge, as it has been reported that AS1411 exists as a mixture of various secondary and tertiary structures in solution.[7] At least eight structural species have been identified in recent decades, ranging from left-handed to right-handed.[7] Apart from stable structures with tracts of three or more continuous guanines ($n \geq 3$), AS1411 is known to possess short G-tracts ($n \leq 2$), which are normally stabilized by the presence of potassium ions that are coordinated by the inward-facing carbonyl groups of G-quadruplexes.[8] Owing to the coexistence of multiple G-quadruplex conformations, the structure of AS1411 has remained unresolved, hindering its development for clinical diagnostics and therapeutics.[7] In contrast, the molecules AT11 and Z-G4, derived from the AS1411 sequence, exhibit similar antiproliferative activity to

Received: November 13, 2024
Revised: February 6, 2025
Accepted: February 9, 2025

AS1411 and possess relatively simpler structures.[9,10] Compared with AS1411, the first guanine in the fourth G-tract of AT11 is replaced by thymine with an additional thymine at both the 5′ and 3′ ends. Nuclear magnetic resonance (NMR) spectroscopy and circular dichroism (CD) spectroscopy suggested that AT11 has a right-handed GQ conformation.[9] Compared with AS1411, the second guanine in the eighth G-tract of Z-G4 is replaced by thymine with an additional thymine at both the 5′ and 3′ ends. NMR spectroscopy and X-ray diffraction revealed a left-handed GQ conformation for Z-G4.[10] To determine the structure(s) of AS1411, it is essential to accurately probe the structural dynamics (particularly individual folding and unfolding behaviors) of AS1411 in solution.

Although various methods, such as NMR spectroscopy,[11,12] CD spectroscopy,[13,14] X-ray diffraction,[15] and electrospray ionization mass spectrometry (ESI-MS),[16] have been used to study structural variants of G-tract motifs, these techniques are suitable only for crystals or measurements in bulk solution and lack temporal and spatial sensitivity, as well as rigidity and resilience under forced conditions. Moreover, they are incapable of detecting AT11 and Z-G4 at the single-molecule level, let alone AS1411. Therefore, advanced techniques are essential for detecting and distinguishing individual AT11 and Z-G4 molecules in solution. Nanopore sensors offer a versatile platform for studying individual biomolecules, providing valuable insights into their structure, dynamics, and interactions. By linearizing and translocating single analyte entities through a tiny pore, this method allows for the measurement of ion flow blockages within physiological electrolytes. Thus, nanopore sensors have been increasingly used in the analysis of single-molecule DNA,[17−20] RNA,[21,22] peptides,[23] and other organic molecules.[24−27] We proposed the detection of AS1411 using the channel protein *Mycobacterium smegmatis* porin A (MspA), which has been widely used for nucleic acid and peptide sequencing.[28] Its short and narrow constriction of approximately 1.2 nm permits the entry of only single-stranded DNA,[29] while its large vestibule of 4.8 nm facilitates interactions with double to four strands, which confers a significant advantage in interactions with GQs compared with alpha-hemolysin (α-HL) with a vestibule of 3.0 nm[30] and aerolysin (AeL) with a vestibule of approximately 1.4 nm.[31,32] Additionally, MspA nanopores in the form of rigid octamers exhibit high stability under elevated temperatures and a broader pH range,[33] enabling the possibility of unfolding AT11 and Z-G4 with appropriate bias voltages.[34] When interrogated with nanopore sensors, MspA is expected to exhibit enhanced temporal resolution and richer electrophoretic/electro-osmotic interactions with AT11 and Z-G4. Recently, MspA has demonstrated efficacy in the detection of short-lived G-quadruplexes.[35]

In this work, we initially investigated two derivatives of the guanine-rich oligonucleotide AS1411, namely, AT11[9] and Z-G4,[10] showcasing the resolving power of MspA. Molecular dynamics (MD) simulations were conducted to examine the interactions of AT11 and Z-G4 with the MspA nanopores under high electric fields, elucidating that the newly formed population (type III) of Z-G4 exhibited significant differences in dwell time and current blockage fraction compared with those of other populations. Electrostatic-field-induced docking and unfolding events, examined by highly confined MspA nanopores, shed light on the structural states, cation-dependent stability, and unwinding dynamics of G-tracts. Moreover, nanopore detection was performed on AS1411 and another of its derivatives, T-AS1411-T, which has an additional thymine at both the 5′ and 3′ ends. Both exhibited only two types of event populations with minimal but reliable differences compared to those of the deterministic derivative AT11. Our work presents a strategy for the rapid discrimination of nucleic acid aptamers with similar sequences, shedding light on the precision of molecular diagnostics and selective targeting in therapeutic applications.

■ MATERIALS AND METHODS

Materials and Chemicals. AT11 (seq #1, TGGTGGTGGTTGTTGTGGTGGTGGTGGT), Z-G4 (seq #2, TGGTGGTGGTGGTTGTGGTGGTGGTGTT), AS1411 (seq #3, GGTGGTGGTGGTTGTGGTGGTGGTGG), and T-AS1411-T (seq #4, TGGTGGTGGTGGTTGTGGTGGTGGTGGT) were synthesized by Tsingke Biotechnology (Beijing, China). ssDNA (seq # 5, GTGTTACCGTGGGAAT-GAATCCTTTTTTTTTTTTTT) was synthesized by GENEWIZ (Suzhou, China). Hexane and hexadecane were purchased from Sigma-Aldrich (Shanghai, China). Octane was purchased from Macklin (Shanghai, China). Sodium chloride (NaCl) was purchased from Sangon Biotech (Shanghai, China). HEPES was purchased from Coolaber (Beijing, China).

Expression and Purification of M2-MspA. The DNA sequence of M2-MspA (D93N/D91N/D90N/D118R/D134R/E139 K) was synthesized and cloned into the pET-30a (+) plasmid to encode the M2-MspA nanopore with a C-terminal hexahistidine tag (His-tag). The protein was expressed in the *E. coli* BL21 (DE3) strain by growing the cells to an absorbance at OD600 of 0.8 and then induced with 0.5 M IPTG. The cells were harvested by centrifugation at 5000*g* after induction at 18 °C overnight.

The pellet was subsequently resuspended in buffer A (15 mM Tris-HCl, 150 mM NaCl, and 10 mM imidazole, pH 7.5) and disrupted by an ultrasonic cell disruptor. The cell debris was removed by centrifugation (10,000*g*) for 10 min. After that, 0.5% OPOE was added to the suspension followed by heating for 30 min at 60 °C. The suspension was cooled on ice for 10 min and centrifuged at 4 °C for 30 min at 13,000*g*. After syringe filtration, the supernatant was applied to a nickel affinity column. The column was washed with 20 column volumes of buffer B (15 mM Tris-HCl at pH 8.0, 150 mM NaCl, 0.5% m/v OPOE, and 40 mM imidazole), and the recombinant protein was eluted with buffer C (15 mM Tris-HCl at pH 8.0, 150 mM NaCl, 0.5% m/v OPOE, and 300 mM imidazole). The fractions were subjected to ultrafiltration through a 100 kDa MWCO filter (Millipore). The M2-MspA octamer was collected, characterized by 12% SDS-PAGE (shown in Figure S4), and used directly for electrophysiology measurements.

Single-Channel Current Recordings. Individual M2-MspA (D90N/D91N/D93N/D118R/E139 K/D134R) nanopores[36] were inserted into a vertical lipid bilayer. The chamber holds a volume of 650 μL on each side and is physically separated by a Teflon film (30 μm thick) with an orifice (ø = 100 μm). The orifice in the film was pretreated with 1% (v/v) hexadecane in pentane and air-dried thoroughly. Both chambers were then filled with the electrolyte buffer (1 M NaCl, 20 mM HEPES, pH 7.3), which was prepared with ultrapure water and filtered through a membrane (0.2 μm, Jinteng) prior to use. 1,2-Diphytanoyl-*sn*-glycero-3-phosphocholine (DPhPC, Avanti Polar Lipids) was then added to the buffer. A self-assembled lipid bilayer spontaneously forms after the liquid is pipetted up and down in the chamber several times. A pair of freshly made Ag/AgCl electrodes were placed on both sides of the chamber, in contact with the aqueous buffer. By convention, the side that is electrically grounded is defined as the cis side, whereas the opposite side is defined as the trans side.

All single-channel recordings were performed by an Axopatch 200B patch clamp amplifier and digitally sampled by a USB-6003 (National Instruments) at a sampling frequency of 50 kHz and low-pass filtered

https://doi.org/10.1021/acsami.4c19806
ACS Appl. Mater. Interfaces XXXX, XXX, XXX−XXX

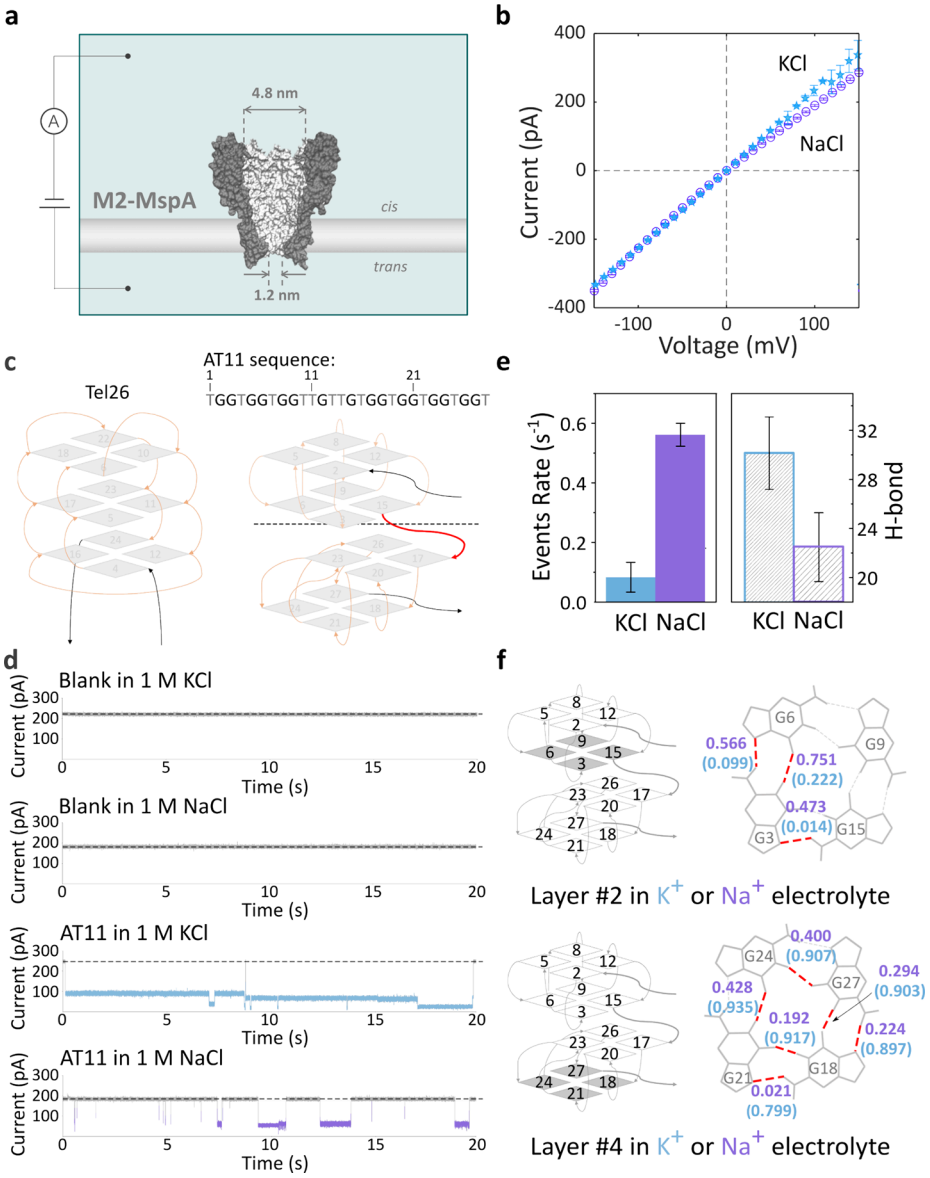

Figure 1. MspA nanopores and cation influenced short G-tract motif interactions. (a) Schematic diagram of M2-MspA nanopore sensing (PDB: 1UUN). (b) Current−voltage relationship of MspA nanopores in 1 M KCl (blue asterisks) and 1 M NaCl (purple circles), together with 20 mM HEPES and pH 7.3. (c) Schematic representation of the folding topology of Tel26 and AT11. (d) Temporal ionic current traces for blank in 1 M KCl, blank in 1 M NaCl, AT11 in 1 M KCl, and AT11 in 1 M NaCl. The baseline (in gray), events for AT11 in 1 M KCl (in blue), and events for AT11 in 1 M NaCl (in purple). (e) Translocation event rates of AT11 and the number of hydrogen bonds of AT11 in 1 M KCl (blue) and 1 M NaCl (purple) solutions. (f) Comparison of hydrogen bond strengths of AT11 in 1 M KCl (blue) and 1 M NaCl (purple) solutions of the second and fourth layer.

with a corner frequency of 10 kHz. The analytes (AT11 or Z-G4) were added to the cis chamber to reach the desired final concentration.

The recorded current traces were filtered with a 2.5 kHz low-pass Bessel filter. Events with dwell times longer than 400 μs were further analyzed. Pyth-Ion (https://github.com/wanunulab/Pyth-Ion) was adapted for postanalysis with a few customized modifications.[37] The key parameters included the dwell time (τ_{dwell}), which is the duration time for single-molecule events; the current blockage ΔI, which is the mean current excluded from the pore by the analyte; and the interevent time dt, from which the DNA capture rates were computed.

Circular Dichroism (CD) Experiments. CD spectroscopy and CD-monitored melting curves were recorded on an Aviv Biomedical spectrometer equipped with a temperature control system using a quartz cuvette with a path length of 1 mm. CD parameters for spectra recording were the following: spectral window 220−320 nm, data pitch 1.0 nm, and bandwidth 1.0 nm. The oligonucleotide sequences were characterized at 25 μM concentrations in Na^+ (1 M NaCl, 20 mM HEPES, pH 7.3) and K^+ (1 M KCl, 20 mM HEPES, pH 7.3) buffer solutions. G-tracts were allowed to form in the oligos by initial denaturation at 95 °C for 5 min followed by slow cooling at room temperature. Thermal denaturation curves were recorded following the CD signal at 263 nm vs the temperature (heating/cooling rate of 1.0 °C/min) in a range of temperatures slightly different depending on saline conditions (15−95 °C for the Na^+ buffer and 20−95 °C for the K^+ buffer).[38] To determine the T_m, CD at variable temperatures was analyzed by first plotting the CD signal at the wavelength of 263 nm against the temperature and then fitting the corresponding plot with a Boltzmann sigmoidal curve implemented in the Origin 2021 software, where the midpoint value x_0 corresponds to T_m (shown in Table S3).[39]

https://doi.org/10.1021/acsami.4c19806
ACS Appl. Mater. Interfaces XXXX, XXX, XXX−XXX

Molecular Dynamics (MD) Simulation. MD simulations were conducted using GROMACS 2022.4[40] with the TIP3P water model[41] and CHARMM36m force field.[42] The entire simulation system was constructed by using the CHARMM-GUI web server[43] for the pores and PACKMOL[44] for the assembly procedure. First, the atomic coordinates of AT11,[9] Z-G4,[10] and MspA[45] were extracted with entries 2N3M, 4U5M, and 1UUN from the Protein Data Bank (PDB), respectively. Next, point mutations of R96A, D93N, D91N, D90N, D118R, D134R, and E139 K (M2-MspA) were introduced into WT-MspA for precise simulation. We then followed the same protocol to add a 1-palmitoyl-2-oleoyl-glycero-3-phosphocholine (POPC) lipid bilayer with dimensions of 12 × 12 nm^2,[46] leading our system to be solvated in a rectangular water box with periodic boundary conditions. Furthermore, the system was established in a symmetric NaCl buffer electrolyte system for the sake of simplicity. Na^+ and Cl^- ions were randomly distributed to achieve a salt concentration of 1 M, followed by a neutralization step. The final system consists of ∼317,000 atoms, where the long-range electrostatic interactions were calculated using the smooth particle-mesh Ewald method.[47] Finally, a cutoff distance of 1.2 nm was used for the calculations of both the short-range electrostatic interactions and the van der Waals interactions, while the covalent bonds involving hydrogen atoms were restrained using the LINCS algorithm.[48]

To simulate AT11 and Z-G4 translocations through thermalized M2-MspA nanopores, each system was first minimized for approximately 4000 steps and then equilibrated at 298 K for 0.25 ns under the NVT (canonical) ensemble using the Berendsen weak-coupling thermostat.[48] Second, the heated systems were equilibrated under the NPT (isothermal−isobaric system) ensemble at 298 K and 1 atm for another 1.75 ns, with the same Berendsen semi-isotropic barostat,[49] resulting in a box geometry of ∼11.6 × 11.6 × 23.1 nm. Third, the translocation simulations were initiated from the final structures of the above equilibration simulations under the NPT ensemble. An external electric field of 4.0 V/10 nm was applied in the direction perpendicular to the membrane plane. Our production simulations lasted for 20 ns with a time step of 2 fs. During the simulations, harmonic positional restraints were applied to the C_α atoms of M2-MspA with a spring constant of 500 $kJ{\cdot}mol^{-1}{\cdot}nm^{-2}$. To observe a full translocation process within a feasible simulation time scale, the external electric field of 4.0 V/10 nm used in the translocation simulations corresponds to a much higher voltage bias than that applied in the experiment. Positional restraints were also applied to avoid the formation of electroporation through the lipid bilayer and to prevent induced ion leakages, which have been reported in the literature even in short MD simulations.[50,51] All the heavy atoms of the lipid molecules were restrained to the positions in the structures obtained from the final equilibrating simulation step under the NPT ensemble by using a harmonic potential with a spring constant of 1000 $kJ{\cdot}mol^{-1}{\cdot}nm^{-2}$. Three independent simulations were performed on AT11 and Z-G4, and the C_α atom of N90 in the eight subunits of the narrowest level of M2-MspA was chosen as the coordinate origin.[46]

■ RESULTS AND DISCUSSION

In-Solution Nanopore Sensing of AT11 Requires Additional Bond Breakages That Can Be Accelerated within Folds. M2-MspA nanopores featuring a wide lumen (4.8 nm) and relatively spacious vestibule are illustrated in Figure 1a. These nanopores can be inserted into the supporting lipid layer, separating the electrolyte into two chambers, cis and trans, and forming ionic flows upon different bias voltages. Figure 1b shows the measured current−voltage relationship of M2-MspA nanopores in their open-pore status for both K^+ and Na^+ cation species. Under positive bias, the pore conductance in 1 M KCl and 1 M NaCl solutions containing 20 mM HEPES to maintain the physiological pH at 7.3 was 2.24 and 1.90 nS, respectively. This 17.9% increase in the open-pore conductance can be elucidated by the specific cation species, given that 1 M KCl and 1 M NaCl exhibit the conductivity of 10.9 and 8.5 S/m,[52] respectively. Nonetheless, under negative biases, an almost identical linear conductance of 2.32 nS was observed. This value was also 3.6 and 22.1% higher than the conductance under positive bias for M2-MspA, indicating that the pore conductance under negative bias is independent of the cation species and might be attributed to other factors, such as conformational changes in M2-MspA.

Since AS1411, with its sequence GGTGGTGGTGGTTGTGGTGGTGGTGG, has been described as exhibiting eight conformations, we initiated our investigation with AT11 (seq: TGGTGGTGGTTGTTGTGGTGGTGGTGGT), a derivative of AS1411 with a single deterministic secondary structure. The sequence has the first guanine in the fourth G_2 of AS1411 replaced by thymine, with an additional thymine at both the 5′ and 3′ ends. Unlike the three G-tetrad layer structure of Tel26,[12] AT11 consists of two units connected by a single nucleotide residue (T16) (Figure 1c),[9] with each unit containing two G-tetrad layers, and the intermediate (second and third) layers of AT11 are more easily exposed to cations.[9]

As electrostatic fields can be built across a nanopore and associated membrane, exerting electrophoretic force onto charged analytes such as DNA and RNA molecules, AT11 could be dragged from the lumen into the vestibule of the pore, thereby contributing to the blockage of ion flow. We measured the ionic current of M2-MspA both with and without AT11 in sodium and potassium cation environments. Temporal current traces were recorded at +100 mV, consistent with conditions commonly reported in the literature,[36,53,54] and are depicted in Figure 1d. Additional results for AT11 in 1 M KCl are listed in Figure S9. The event duration for AT11 in potassium ions ranged from a few seconds to several tens of seconds (shown in blue), whereas the dwell time of events in sodium ions was significantly shorter (shown in purple). This indicates that potassium ions (K^+) could stabilize guanine-rich structures more effectively than sodium ions (Na^+), supported by our CD melting experiments (Figures S7 and S8) and consistent with previous studies.[38] In the K^+ environment, AT11 would exhibit greater structural stability and unfolding resistance, preventing translocation through the nanopore. Instead, it may remain lodged in the vestibule of MspA, leading to a prolonged decrease in the ionic current baseline. Moreover, the event rate of AT11 in KCl solution (blue) was 0.08 ± 0.05 s^{-1}, while in NaCl solution (purple), it increased 6-fold to 0.56 ± 0.04 s^{-1}, as shown in Figure 1e. This phenomenon can be attributed to the higher structural stability of the G-tracts in the potassium ion environment.

For these two cation conditions, we conducted MD simulations thermalized in the corresponding electrolytes to elucidate the details of the associated ions and hydrogen bonds. AT11 was found to maintain an average of 30 ± 3 H-bonds in the potassium ion solution, whereas 22 ± 3 H-bonds were observed in the sodium ion solution. As shown in Figure 1f, our MD simulations suggested that the eight missing hydrogen bonds primarily involve the two layers near the 3′ end and their bond strength, determined by the frequency of hydrogen bond formation between adjacent guanines in each guanine tetrad layer of the G-tract structure over a simulation period of 100,000 ps (as depicted in Figure S1). This finding supported the notion that AT11 could be more susceptible to unfolding its structure in a 1 M NaCl solution than a 1 M KCl solution, which is consistent with our experimental validation.

https://doi.org/10.1021/acsami.4c19806
ACS Appl. Mater. Interfaces XXXX, XXX, XXX−XXX

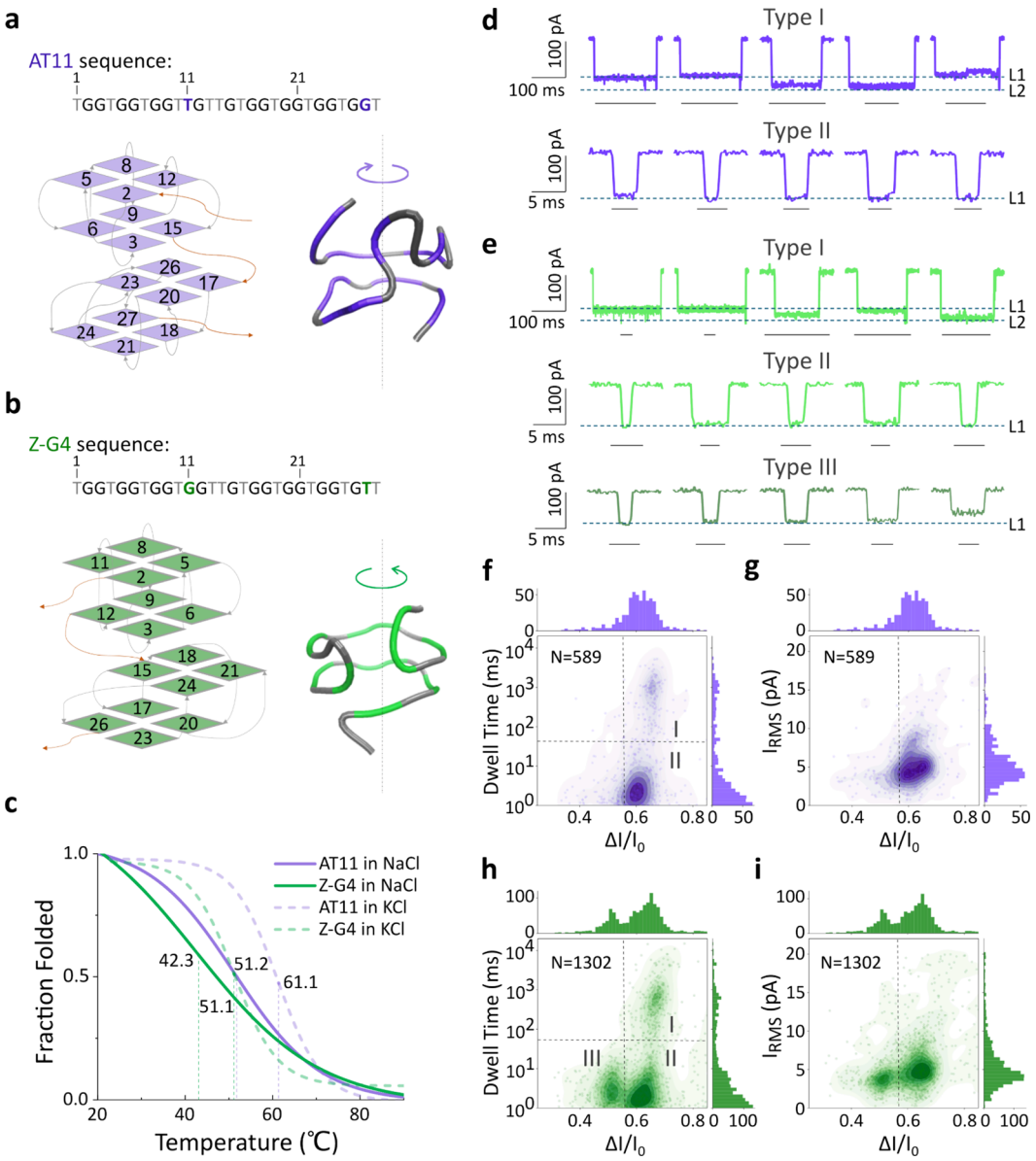

Figure 2. Experimental verification of AT11 and Z-G4 events using M2-MspA nanopores at +100 mV. Sequential illustration, folding topology, and molecular structures of AT11 (right-handed, a) and Z-G4 (left-handed, b) (PDB: 2N3M and 4U5M) thermalized in the 1 M NaCl solution as basket folds. (c) CD-melting profiles of AT11 and Z-G4 in 1 M NaCl solution. Examples of temporal current traces for AT11 (d) and Z-G4 (e). Scale bars for type I are 100 ms, while these are 5 ms for types II and III. Scatter plots of average current blockage fraction ($\Delta I/I_0$) versus dwell time (τ_{dwell}) for AT11 (f) and Z-G4 (h). Scatter plots of $\Delta I/I_0$ versus root-mean-square event current (I_{RMS}) for AT11 (g) and Z-G4 (i). All experiments were performed in 1 M NaCl, 20 mM HEPES, and pH 7.3. All the data were recorded at 10 kHz and filtered at 2.5 kHz.

Consequently, on the basis of the significantly higher event rates, we proceeded with further investigations with G-tracts in sodium ion solution.

A New Population Emerges for the Z-G4 in Sodium Ion Solution. Here, we introduced Z-G4 (seq: TGGTGGTGGTGGTTGTGGTGGTGGTGTTTT), a second derivative with the second guanine in the eighth G_2 of AS1411 replaced by thymidine and an additional thymine at both the 5′ and 3′ ends. Figure 2a,b compares the sequences and structural disparities of these two derivatives. Both AT11 and Z-G4 molecules are regarded as derivative sequences of AS1411. AT11 featured three G_2 at the 5′ end and four G_2 at the 3′ end, while Z-G4 comprised four G_2 at the 5′ end and three G_2 at the 3′ end. This resulted in completely distinguished right-handed (AT11) and left-handed (Z-G4) structures. Both structures have been previously characterized via NMR and crystallography with potassium ions[9,10] but not with sodium ions. To validate this, we performed ultraviolet circular dichroism (UV-CD) measurements with sodium ions. Figures S5 and S6 present the UV-CD spectra of AT11 and Z-G4 in 1 M NaCl and 1 M KCl, respectively. Both spectra exhibit a common spectral pattern with a negative valley at 240 nm and a strong positive peak at 260 nm, typical of right-handed parallel folding.[55,56] Additionally, in 1 M NaCl, a positive band around 290 nm suggests that AT11 and Z-G4 may contain a small fraction of antiparallel folding.[55,56] Our CD results differ from those reported by Phan et al.,[10] who found that Z-G4 adopts a left-handed parallel conformation in the presence of K^+. This discrepancy might be ascribed to variations in the K^+ concentration and differences in the

https://doi.org/10.1021/acsami.4c19806
ACS Appl. Mater. Interfaces XXXX, XXX, XXX−XXX

buffering systems utilized. Figure 2c presents the CD-melting curves of AT11 and Z-G4 in both 1 M NaCl and 1 M KCl. The T_m values of both sequences in Na^+ buffer are lower than in the K^+ buffer, consistent with literature[38] reports that K^+ stabilizes GQ structures more effectively. Notably, while the melting temperature of AT11 (approximately 51.2 °C in Na^+ buffer and 61.1 °C in K^+ buffer) is higher than that of Z-G4 (42.5 °C in Na^+ buffer and 51.1 °C in K^+ buffer), the transition phase of AT11's melting curve is steeper than that of Z-G4. This indicates that AT11 has faster unfolding dynamics and lower structural resilience than Z-G4.

Figure 2d,e presents single-molecule recordings of AT11 and Z-G4 in M2-MspA nanopores. Type I events (with τ_{dwell} centered at 497.28 ms) and type II events (with τ_{dwell} centered at 2.14 ms) for AT11 span durations from hundreds of milliseconds to a few milliseconds, as shown in Figure 2d. The longer duration could indicate molecules undergoing unwinding and being translocated through the pore, as proposed in previous studies,[57] while the shorter duration may point toward the DNA failing to pass through the nanopore.[58] These interpretations are also supported by the voltage dependence of such dwell times (Figure S11). Furthermore, most type I events are characterized by a sustained intermediate current level followed by a deep blockage, providing further evidence for the translocation of AT11 through the pore.[19,20,58−61] Conversely, type II events exhibit a brief intermediate current level, supporting the most plausible view that AT11 molecules could enter the nanopore vestibule before rapidly bouncing back to the *cis* chamber due to thermal motions.[19,20,59,60,62] However, three types of event examples for Z-G4 are illustrated in Figure 2e. The type I and type II events of Z-G4 exhibit ionic current modulation patterns consistent with those observed in AT11, respectively. These behaviors likely correspond to similar dynamic processes. Among the five selected type I events, events 1, 2, and 5 for AT11 (and events 1, 2, and 4 for Z-G4) are characterized by a prolonged intermediate current level followed by a brief deep current blockage; events 3 and 4 for AT11 (and events 3 and 5 for Z-G4 type I) exhibit only a prolonged deep current blockage. These distinct current modulation patterns are likely attributable to differences in the translocation orientation of G-rich molecules through the nanopore. Specifically, the former pattern may point toward translocation of G-rich DNA molecules with their 5′ end entering the nanopore, whereas the latter pattern could reflect translocation with the 3′ end leading. This hypothesis is supported by the observation that the current blockage ratio is slightly higher when DNA enters the nanopore from the cis side with the 3′ end compared to the 5′ end.[63,64] The statistical results of the scatter plots of the dwell time (τ_{dwell}) and the average current blockage fraction ($\Delta I/I_0$) are summarized in Figure 2f,h (N = 589 and 1302), which can be roughly divided into four regions. Type I events for AT11 exhibited a dwell time predominantly at 497.28 ms with an average current blockage fraction ($\Delta I/I_0$) of 65.5%. For Z-G4, the dwell time distribution was predominantly at 316.23 ms, with an average current blockage fraction of 66.5%. This extended duration could be attributed to the alignment of the 3′ and 5′ ends toward the constriction zone and the time-consuming unfolding process.[58,65] Type II events (τ_{dwell} < 50 ms and $\Delta I/I_0$ > 0.55) showed an average current blockage fraction of 61.5% for AT11 and 63.6% for Z-G4. The shorter duration may point toward certain factors, such as an improper docking orientation, that would prevent further unfolding,[59,62,65] as supported by the voltage-dependence results (shown in Figure S11). However, the underlying mechanisms may still require further investigations. The third type of event for Z-G4 ($\Delta I/I_0$ < 0.55) had an average current blockage fraction of 52.5%. This formed a new population in the scatter plot of $\Delta I/I_0$ versus the root-mean-square current (I_{RMS}) in Figure 2i compared with that of AT11 in Figure 2g. We propose that this population represents the emergence of a new state, possibly because the structure of Z-G4 is more resistant to unwinding, leading to more frequent collision rather than translocation events under an electric field force. This resulted in a shallow current blockage fraction, slightly exceeding half of the baseline level, which is likely attributed to interactions in the vestibule of the pore,[58] as shown in Figure 2h. Additionally, the "resilience" nature of Z-G4 also led to a fast dwell time for this population, reflecting the nature of shallow docking inside the nanopore as a rapid, reversible process.

Elongated Interactions of Z-G4 Are Observed with Increasing Bias Voltages. Considering that the voltage-dependent dynamics of the interactions between AT11 and Z-G4 with the M2-MspA nanopore may provide further insights into these events, we recorded and analyzed the ionic currents of DNA experiments ranging from +100 to +160 mV in Figure 3, including the mean and standard deviation of the normalized

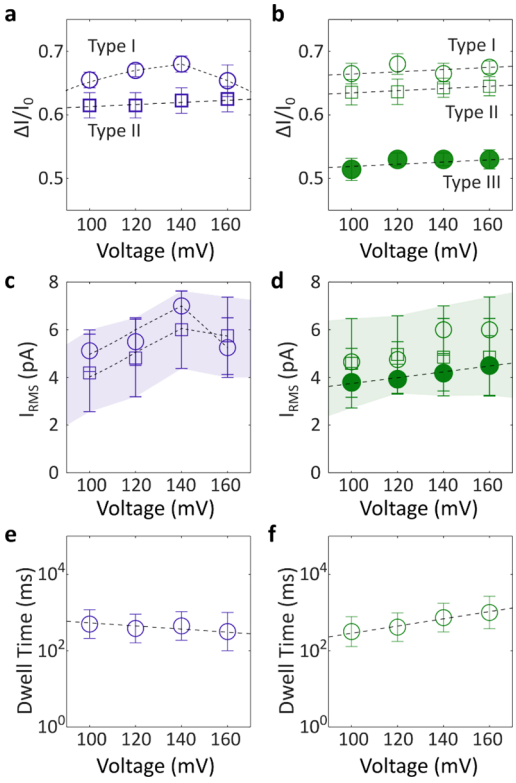

Figure 3. Voltage-dependent dynamics of AT11 and Z-G4 interactions with the M2-MspA nanopore. Average current blockage fraction ($\Delta I/I_0$) as a function of bias voltage for AT11 (a) and Z-G4 (b). Root-mean-square event current (I_{RMS}) as a function of bias voltage for AT11 (c) and Z-G4 (d). Dwell time as a function of bias voltage for AT11 (e) and Z-G4 (f). Type I, II, and III events were labeled with circles, squares, and solid dots, whereas the dash lines indicate linear fittings of the events. All experiments were performed in 1 M NaCl, 20 mM HEPES, and pH 7.3. All the data were recorded at 10 kHz and filtered at 2.5 kHz.

https://doi.org/10.1021/acsami.4c19806
ACS Appl. Mater. Interfaces XXXX, XXX, XXX−XXX

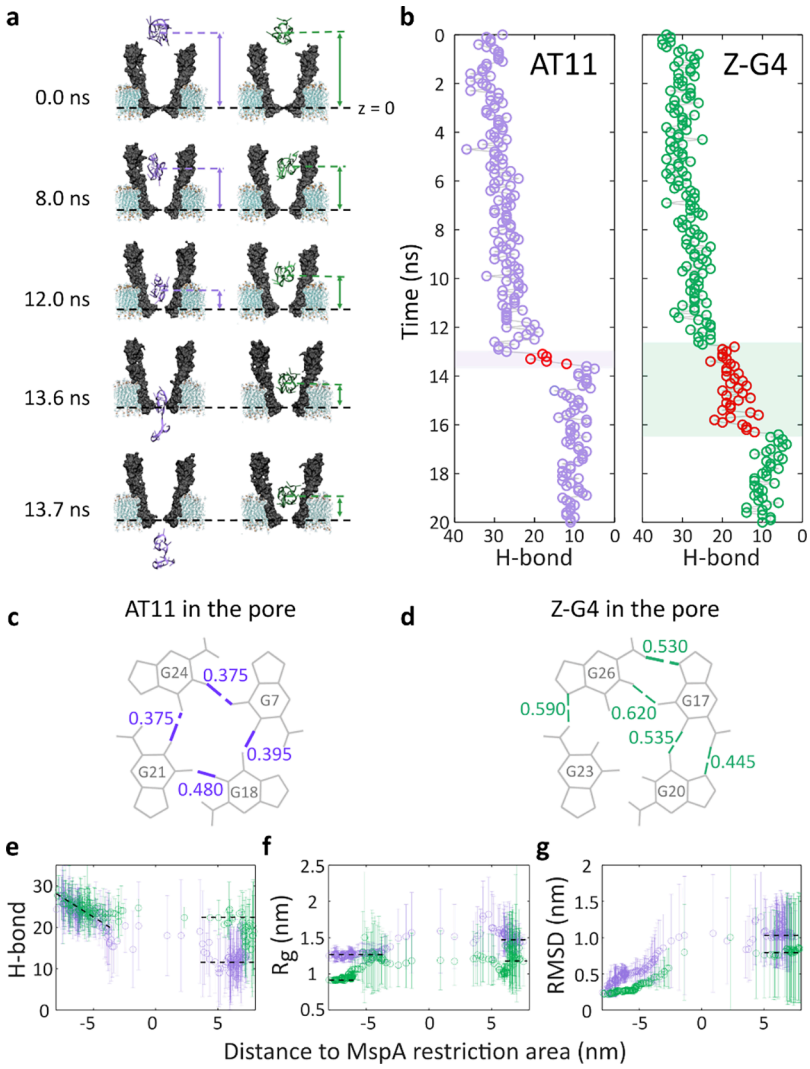

Figure 4. Molecular dynamics of AT11 and Z-G4 events through M2-MspA nanopores. (a) Equilibrated structures of AT11 and Z-G4 entering an M2-MspA nanopore. (b) Number of hydrogen bonds as a function of time for AT11 and Z-G4. Comparison of the fourth layer's hydrogen bond strengths of AT11 (c) and Z-G4 (d) when translocated through the M2-MspA nanopore. The number of hydrogen bonds (e), gyration radius (R_g) (f), and root-mean-square distance (RMSD) (g) of AT11 and Z-G4 as functions of relative positions to the M2-MspA restriction area.

current deviation ($\Delta I/I_0$), current noise (I_{RMS}), and dwell time (τ_{dwell}). The type I events for AT11 exhibited a decrease in $\Delta I/I_0$ at +160 mV, as shown in Figure 3a, which was also manifested in I_{RMS} in Figure 3c. We believe that the observed current blockage phenomenon at +160 mV for AT11 is likely related to its structural characteristics, indicating a biphasic voltage dependence. Below the threshold voltage of 140 mV, as the voltage increases, the interaction between AT11 and the nanopore within the vestibule intensifies, resembling a crowding effect[66] that explains the observed increase in current blockage ($\Delta I/I_0$) for type I events. However, above the threshold voltage, AT11 experiences a stronger interaction with the MspA vestibule, leading to rapid structural unfolding and reduced ion flow blockage, resulting in a slight decrease in the current blockage ($\Delta I/I_0$) for type I events. This observation is consistent with the structural resilience of AT11 as reflected by the temperature melting curve. Unlike this mechanism, the nonmonotonic voltage dependence observed in PNA3-DNA1 arises from dynamic adjustments in charge distribution within the duplex and its positional changes inside the nanopore as the voltage increases.[67] The hypothesis could involve the following: at lower voltages, the interaction between AT11 and the nanopore is relatively weak, but as the voltage increases, the interaction strengthens, leading to a gradual increase in both current blockage ratio and noise. Once the voltage surpasses a certain threshold, frequent and intense collisions between AT11 and the nanopore may cause structural deformation, resulting in a subsequent decrease in both the current blockage ratio and noise. Furthermore, the voltage-dependent dynamics of AT11 reveals that type I events exhibit greater current blockage at 120 mV, significantly differing from that of type II events. We believe that 120 mV would be a better choice in further distinguishing structural variants of irregular DNA G-rich motifs. It is worth noting that a similar trend was not observed in the dwell time, which may be due to the dual influence of structural characteristics and the electric field. Increasing the applied voltage enhances the electric force on the G-tracts, which accelerates their unfolding and translocation, thereby reducing the dwell time. This may be analogous to the voltage-dependent behavior described by Wang et al.[22] Our experimental results indicate that the effect of the applied

https://doi.org/10.1021/acsami.4c19806
ACS Appl. Mater. Interfaces XXXX, XXX, XXX−XXX

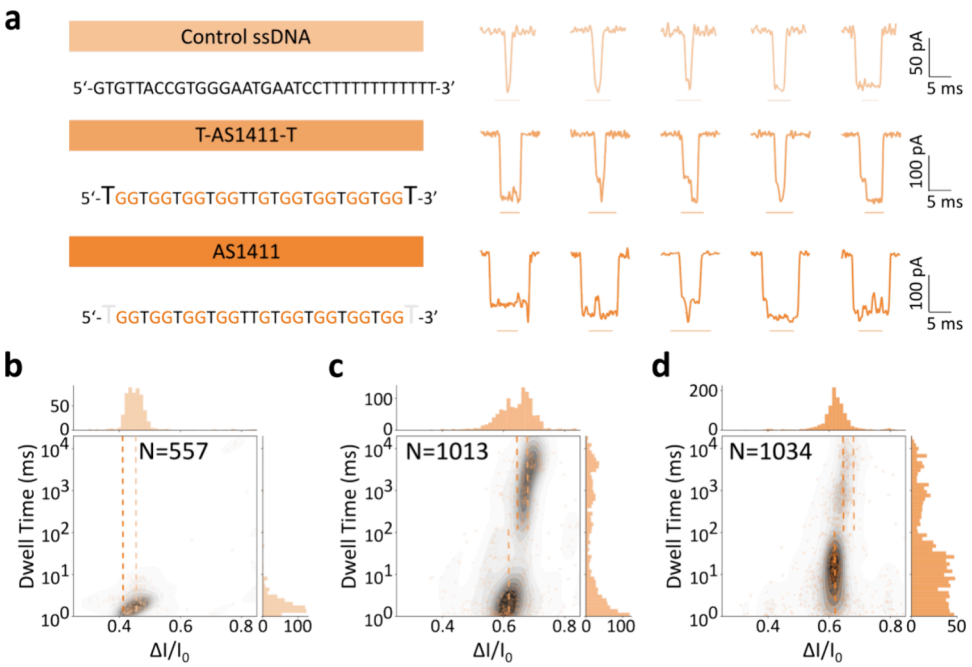

Figure 5. M2-MspA nanopore recordings of AS1411 and derivatives. (a) Sequential presentation and typical event Illustrations. Scatter plots of average current blockage fraction ($\Delta I/I_0$) versus dwell time of control ssDNA (b), T-AS1411-T (c), and AS1411 (d). All experiments were performed in 1 M NaCl, 20 mM HEPES, and pH 7.3. All the data were recorded at +100 mV and 10 kHz and filtered at 2.5 kHz.

voltage on dwell time is dominant for AT11. At 100 mV, type I events exhibit deeper blockages, indicating more significant interactions similar to those observed during complete pore translocation. A decrease in the dwell time with increasing bias voltage was observed in Figure 3e, indicating, to some extent, the accelerated unzipping and translocation of the right-handed two bilayer stacks. In contrast, the type II event duration exhibits weak voltage dependence (Figure S11), suggesting that AT11 may escape back to the cis chamber rather than translocate through the pore, as corroborated by previous literature.[22,58]

Nevertheless, the $\Delta I/I_0$ of the first two types for Z-G4 in Figure 3b was slightly higher than AT11. The $\Delta I/I_0$ of type III events showed a slight increase with increasing bias voltage, which may be explained by stronger electrostatic fields enhancing the interaction between Z-G4 and the nanopore, increasing the probability of pulling the molecule into a deeper position in the vestibule. Due to the distribution differences in I_{RMS} in Figure 3d and Figure S10, one could expect considerable possible orientations and structural changes of Z-G4 as it passed through a pore, warranting further investigation. Last but not least, Figure 3f depicts an increasing dwell time for type I events, indicating prolonged interactions between Z-G4 and MspA. This observation suggested that with increasing bias voltage, although the interaction between Z-G4 and the nanopore strengthens, the slow or difficult unfolding of the Z-G4 structure leads to greater resistance during translocation. This further suggests that Z-G4 has a greater structural resilience than AT11, as supported by the CD melting curve (Figure S7). The type II and type III events for Z-G4 exhibit a stronger monotonic increase with voltage (Figure S11), indicating that the escape process may be far more sensitive to voltage than the threading process. The relatively weaker voltage dependence of threading could be attributed to the small voltage gradient within the vestibule and the absence of negatively charged terminal phosphate groups at both the 3′ and 5′ ends of our synthetic polymers.[66]

Molecular Dynamics Simulations Suggest Prolonged Docking Interactions of Z-G4. To gain insight into the interactions between the G-tract motifs and the nanopore, we performed all-atom MD simulations within M2-MspA, as illustrated in Figure 4a. The centroids of both AT11 and Z-G4, initially not in direct contact with MspA, were positioned at the same height at the top of the lumen at 0.0 ns. An individual AT11 was driven into the lumen and temporarily docked at 12.0 ns and then underwent unwinding at 13.6 ns. Meanwhile, an example of a Z-G4 molecule gave rise to an extended stay in the vestibule. Figure 4b depicts the hydrogen bonds inside the G-tracts of AT11 and Z-G4, leading to a rapid transition from 21 to 7 H-bonds in less than 1.3 ns for AT11, while taking 3.5 ns for Z-G4, with two distinct stages featuring 19 and 10 H-bonds. We posited that this significant time difference between the two could stem from the susceptibility of the fourth layer instead of other layers (Figures S2 and S3) in Figure 4c,d. This layer of AT11 appeared to be more susceptible to ion-induced damage than that of Z-G4.

The H-bonds, radius of gyration, and root-mean-square distance (RMSD) of the molecule were then analyzed as a function of the position relative to the constriction of M2-MspA in Figure 4e−g. In Figure 4e, both AT11 and Z-G4 exhibited similar decreasing slopes of H-bonds upon entering the pore and its vestibule. After the translocation process, Z-G4 rapidly formed approximately 22 H-bonds, while AT11 remained at around 12. This spontaneous reformation of 10 additional H-bonds for Z-G4 supported the fact that the unwound process of Z-G4 ought to be time-consuming.

Figure 4f shows the radius of gyration for AT11 and Z-G4. On the one hand, Z-G4 was found to have a reasonably smaller radius, ranging from 0.97 to 1.23 nm, when translocating through the pore. On the other hand, AT11 had a larger (radius of gyration) R_g of 1.17 to 1.82 nm, advocating for a

https://doi.org/10.1021/acsami.4c19806
ACS Appl. Mater. Interfaces XXXX, XXX, XXX−XXX

greater degree of freedom in rotations that may occur inside the pore. Such flipping or rotating actions may contribute to quick searches for unwinding opportunities when the molecule is docked in the vestibule.

The RMSD values in Figure 4g display the resilience of the G-tract motifs. Both AT11 and Z-G4 were tightly packed inside the pores and gradually became disturbed. As they were linearized and translocated through the pore, the RMSD increased for both. The RMSD variations of both AT11 and Z-G4 corresponded with changes in their respective H-bond numbers, indicating that the breaking and formation of H-bonds were the direct causes of the disruption and reformation of these two G-tract structures. The consistently lower RMSD of Z-G4 compared to AT11 indicated a more compact structure with greater resistance to linearization. Conversely, the ease of linearization of the AT11 structure may result in a lack of docking populations.

AS1411 in Sodium Ion Solution Is Inclined to Be Unfolded as AT11. In addition to discriminating between two isomers, structural examinations were performed on AS1411 and its analogs. Figure 5a displays the sequences of single-strand DNA as a control (34 bp, control ssDNA), T-AS1411-T, and AS1411 itself, along with five representative events for each. Figure 5b−d shows the distributions of the average current blockage fraction ($\Delta I/I_0$) and dwell time (τ_{dwell}) for the events of these sequences. Since the control ssDNA could not form G-quadruplex structures and may adopt randomly coiled secondary structures, a population of short-lived (1.78 ms) and shallow current drop (46.3%) was observed in Figure 5b ($N = 557$). With two thymine extensions on both the 5′ and 3′ ends, T-AS1411-T was precisely comparable with AT11 and Z-G4, which both exhibited only a single nucleotide mutation from T-AS1411-T. Figure 5c ($N = 1013$) shows two event populations for T-AS1411-T. Type I events had an average current blockage fraction of 67.6%, while that of type II events was primarily 62.4%. This showed a minor difference compared with AT11 in Figure 3c but a significant difference compared with Z-G4 in Figure 3d. AS1411 differs from T-AS1411-T by having one less thymine at both the 5′ and 3′ ends. According to Figure 5d ($N = 1034$), AS1411 exhibited only two types of events. Type I events had an average current blockage fraction that was 4.6% lower than that of T-AS1411-T, and type II events had a dwell time that was nearly 10 ms longer than that of T-AS1411-T.

Dissociation Discrepancies Induced by Sequence and Termini. The extracted $\Delta I/I_0$ at 100 mV are listed in Table 1 for comparison, whereas the extracted I_{RMS} and τ_{dwell} are provided in Tables S1 and S2. Type III events exhibited a 46.3% blockage, suggesting molecular docking rather than translocation through the M2-MspA nanopore, which would show an average current blockage fraction greater than 64%, with additional deeper blockages of 5−15% toward the end of the event.[54] For Z-G4, the formation of two relatively rigid bilayer stacks contributed to three deeper blockages: transient events with average current blockage fractions of 52.5 and 63.6% likely indicated docking at the upper and inner vestibules, respectively, while events with an average current blockage fraction of 65.5% suggested docking closer to the constriction region of the pore followed by translocation through the nanopore. In contrast, AT11, being less resilient in a sodium ion environment, lacked type III events and only exhibited type I and type II events, with average current blockage fractions that were 1.0 and 2.1% lower than those of Z-G4, respectively.

Table 1. Extracted $\Delta I/I_0$ for Measured Oligonucleotides in 1 M NaCl

	type I	type II	type III
control ssDNA			0.463 ± 0.040
Z-G4	0.665 ± 0.033	0.636 ± 0.040	0.525 ± 0.050
AT11	0.655 ± 0.025	0.615 ± 0.040	
T-AS1411-T	0.676 ± 0.025	0.624 ± 0.044	
AS1411	0.645 ± 0.020	0.625 ± 0.040	

T-AS1411-T, on the other hand, can be discriminated from AT11 by the blockage increment of 0.9% of type II events. This might be attributed to T-AS1411-T, which has a similar number of hydrogen bonds but a much more compact R_g and RMSD than AT11. Surprisingly, AS1411 itself had almost the same type II events as T-AS1411-T but a 3.1% reduction in the blockage of type I. This finding indicated that the removal of terminal thymine was not favorable for AS1411 to adopt an orientation suitable for nanopore translocation. Notably, in Na^+ buffer, the T_m of T-AS1411-T is higher than that of AS1411, and its melting curve shows a more gradual transition (as shown in Figure S7), indicating greater structural resilience. This result is inconsistent with the findings from the nanopore experiments. We propose that this discrepancy is due to the fundamental differences between the two methodologies. In nanopore experiments, the G-tract structure interacts with the nanopore, and the thymine extensions at the ends of T-AS1411-T facilitate this interaction, making it more prone to unfolding and translocation compared to AS1411. In contrast, the CD thermal melting experiment does not involve such interactions with other molecules.

CONCLUSIONS

Guanine-rich sequences with short G-tracts ($n \leq 2$) that interacted with M2-MspA nanopores were discriminated statistically and investigated via histograms at the single-molecule level. Molecular dynamics simulations suggested that sodium ions played a key role in the reversible breaking of hydrogen bonds within the double layer. Single-channel nanopore experiments showed that the event rate of AT11 in NaCl solution increased 6-fold compared with that in KCl solution, increasing from 0.08 ± 0.05 to 0.56 ± 0.04 s^{-1}.

The presence of thymine ends proved crucial for the unwinding of AS1411, as evidenced by the differentiation with an −4.6% shift. Although AS1411 was known to have eight types of structures resolved by NMR, there were only two populations of events associated with the interaction of AS1411 with M2-MspA, showing minimal differences compared to those of deterministic derivatives AT11 (0.655 ± 0.025 vs 0.645 ± 0.020 and 0.615 ± 0.040 vs 0.625 ± 0.040). While the differences for individual events are minimal, one can achieve statistical significance rapidly and therefore identify these sequence-similar variants due to the high abundance of events observed in nanopore detection. More surprisingly, the other derivative, Z-G4, exhibited a new type of event in the scatter plot. This can be attributed to the reduced susceptibility of its fourth layer and the consequent increased rigidity, facilitating rapid docking in the nanopore.

Furthermore, increasing the bias voltage significantly extends the dwell time of type I events for Z-G4 to approximately 1000 ms, indicating its higher sensitivity in comparison to AT11,

https://doi.org/10.1021/acsami.4c19806
ACS Appl. Mater. Interfaces XXXX, XXX, XXX−XXX

which remains stable at approximately 100 ms. These findings demonstrate the potential of M2-MspA for rapidly distinguishing various G-tracts including their structural variants, cation-dependent stability, and unwinding dynamics. Overall, our pieces of knowledge extracted from nanopore experiments contribute to setting a precedent for investigations of the AS1411 aptamer and its derivatives under native-like conditions. This could open an avenue toward applications in the preliminary evaluation of structural properties and unfolding dynamics of nucleic-acid-based therapeutics, as well as in the rapid screening of similar aptamers using nanopores.

■ ASSOCIATED CONTENT

Supporting Information

The Supporting Information is available free of charge at https://pubs.acs.org/doi/10.1021/acsami.4c19806.

Comparison of hydrogen bond strengths of AT11 in NaCl and KCl solutions; hydrogen bond strengths of AT11 and Z-G4 during translocation through MspA nanopores; gel image of M2-MspA; circular dichroism spectra and melting curves of measured oligonucleotides in NaCl and KCl solutions; extracted I_{RMS} and τ_{dwell} values of measured oligonucleotides (table); and T_m values of measured oligonucleotides in NaCl and KCl solutions (table) (PDF)

■ AUTHOR INFORMATION

Corresponding Authors

Ronghui Liu − *School of Microelectronics, MOE Engineering Research Center of Integrated Circuits for Next Generation Communications, Southern University of Science and Technology, Shenzhen 518055, China;* orcid.org/0009-0003-7763-8766; Email: liurh@sustech.edu.cn

Yao Li − *School of Physics and Key Laboratory of Functional Polymer Materials of Ministry of Education, Nankai University, and Collaborative Innovation Center of Chemical Science and Engineering, Tianjin 300071, China;* orcid.org/0000-0002-7926-7597; Email: liyao@nankai.edu.cn

Yi Li − *School of Microelectronics, MOE Engineering Research Center of Integrated Circuits for Next Generation Communications, Southern University of Science and Technology, Shenzhen 518055, China;* orcid.org/0000-0002-6134-3117; Email: liy37@sustech.edu.cn

Authors

Jiadun Liu − *School of Microelectronics, MOE Engineering Research Center of Integrated Circuits for Next Generation Communications, Southern University of Science and Technology, Shenzhen 518055, China;* orcid.org/0009-0005-7195-1457

Luoan Xiong − *School of Physics and Key Laboratory of Functional Polymer Materials of Ministry of Education, Nankai University, and Collaborative Innovation Center of Chemical Science and Engineering, Tianjin 300071, China*

Yuhang Hu − *School of Microelectronics, MOE Engineering Research Center of Integrated Circuits for Next Generation Communications, Southern University of Science and Technology, Shenzhen 518055, China;* orcid.org/0009-0007-3114-6749

Zhuofei Wang − *School of Microelectronics, MOE Engineering Research Center of Integrated Circuits for Next Generation Communications, Southern University of Science and Technology, Shenzhen 518055, China; State Key Laboratory of Medicinal Chemical Biology, College of Pharmacy, Nankai University, Tianjin 300350, China*

Jing Dai − *School of Microelectronics, MOE Engineering Research Center of Integrated Circuits for Next Generation Communications, Southern University of Science and Technology, Shenzhen 518055, China; School of Public Health, Guangdong Medical University, Dongguan 523808, China*

Tie Li − *Department of Biology, School of Life Sciences, Southern University of Science and Technology, Shenzhen 518055, China*

Xinrong Guo − *School of Public Health, Guangdong Medical University, Dongguan 523808, China;* orcid.org/0000-0001-9532-0506

Zhongbo Yu − *State Key Laboratory of Medicinal Chemical Biology, College of Pharmacy, Nankai University, Tianjin 300350, China;* orcid.org/0000-0002-0634-554X

Complete contact information is available at: https://pubs.acs.org/10.1021/acsami.4c19806

Author Contributions

‡J.L., L.X., and Y.H. contributed equally. Yi L., Yao L., and R.L. conceived and designed the experiments. Yi L. directed the project. J.L. and Y.H. performed the experiments. L.X. conducted all-atom molecular dynamics (MD) simulations. Z.W., J.D., and T.L. contributed to the preparation of the M2-MspA protein. J.L. and Y.H. analyzed the data and wrote the manuscript. X.G. and Z.Y. provided suggestions for manuscript writing. J.L., R.L., and Yi L. wrote and revised the manuscript. All the authors discussed the results and commented on the manuscript.

Funding

J.L., Y.H., Z.W., J.D., T.L., R.L. and Yi L. acknowledge the support from the Ministry of Science and Technology of China (2022YFF1203400), the National Natural Science Foundation of China (grant 62171211), the Science and Technology Innovation Commission of Shenzhen (JCYJ20220814170440001, JCYJ202208183000194, and JCYJ202205303000329), and NSQKJJ under grants K21799109 and K21799116. R.L. acknowledges the support from the National Natural Science Foundation of China (32371526 and 32100021) and the Science and Technology Innovation Commission of Shenzhen (JCYJ20230807092459028). L.X. and Yao L. also acknowledge the support from the National Natural Science Foundation of China (12275137) and Fundamental Research Funds for the Central Universities, Nankai University (63221053 and 63231190).

Notes

The authors declare no competing financial interest.

■ ACKNOWLEDGMENTS

The authors thank Prof. Yi-Tao Long's group for their generous help with the experimental setups, Ms. Zichun Li for her preliminary experiments of M2-MspA insertions and DNA translocations, as well as Ms. Rui Guo for her help with the MD simulations. Lastly, all authors declare no competing interest.

REFERENCES

(1) Guédin, A.; Lin, L. Y.; Armane, S.; Lacroix, L.; Mergny, J.-L.; Thore, S.; Yatsunyk, L. A. Quadruplexes in '*Dicty*': crystal structure of a four-quartet G-quadruplex formed by G-rich motif found in the Dictyostelium discoideum genome. *Nucleic Acids Res.* **2018**, *46* (10), 5297−5307.

(2) Phan, A. T.; Kuryavyi, V.; Luu, K. N.; Patel, D. J. Structure of two intramolecular G-quadruplexes formed by natural human telomere sequences in K^+ solution. *Nucleic Acids Res.* **2007**, *35* (19), 6517−6525.

(3) Patel, D. J.; Phan, A. T.; Kuryavyi, V. Human telomere, oncogenic promoter and 5′-UTR G-quadruplexes: diverse higher order DNA and RNA targets for cancer therapeutics. *Nucleic Acids Res.* **2007**, *35* (22), 7429−7455.

(4) Safarzadeh Kozani, P.; Safarzadeh Kozani, P.; Malik, M. T. AS1411-functionalized delivery nanosystems for targeted cancer therapy. *Explor. Med.* **2021**, *2* (2), 146−166.

(5) Alizadeh, L.; Alizadeh, E.; Zarebkohan, A.; Ahmadi, E.; Rahmati-Yamchi, M.; Salehi, R. AS1411 aptamer-functionalized chitosan-silica nanoparticles for targeted delivery of epigallocatechin gallate to the SKOV-3 ovarian cancer cell lines. *J. Nanopart. Res.* **2020**, *22* (1), 5.

(6) Lin, J.; Wang, X.; Ni, D.; Chen, Y.; Chen, C.; Liu, Y. Combinational Gene Therapy toward Cancer with Nanoplatform: Strategies and Principles. *ACS Materials Au.* **2023**, *3* (6), 584−599.

(7) Dailey, M. M.; Miller, M. C.; Bates, P. J.; Lane, A. N.; Trent, J. O. Resolution and characterization of the structural polymorphism of a single quadruplex-forming sequence. *Nucleic Acids Res.* **2010**, *38* (14), 4877−4888.

(8) Rachwal, P. A. Effect of sequence on the folding and stability of DNA G-quadruplexes. Ph. D. Dissertation, University of Southampton, 2008, http://eprints.soton.ac.uk/id/eprint/466531 (accessed 2024−03−16).

(9) Do, N. Q.; Chung, W. J.; Truong, T. H. A.; Heddi, B.; Phan, A. T. G-quadruplex structure of an anti-proliferative DNA sequence. *Nucleic Acids Res.* **2017**, *45* (12), 7487−7493.

(10) Chung, W. J.; Heddi, B.; Schmitt, E.; Lim, K. W.; Mechulam, Y.; Phan, A. T. Structure of a left-handed DNA G-quadruplex. *Proc. Natl. Acad. Sci. U.S.A.* **2015**, *112* (9), 2729−2733.

(11) Luu, K. N.; Phan, A. T.; Kuryavyi, V.; Lacroix, L.; Patel, D. J. Structure of the human telomere in K^+ solution: an intramolecular (3 + 1) G-quadruplex scaffold. *J. Am. Chem. Soc.* **2006**, *128* (30), 9963−9970.

(12) Ambrus, A.; Chen, D.; Dai, J.; Bialis, T.; Jones, R. A.; Yang, D. Human telomeric sequence forms a hybrid-type intramolecular G-quadruplex structure with mixed parallel/antiparallel strands in potassium solution. *Nucleic Acids Res.* **2006**, *34* (9), 2723−2735.

(13) Dash, J.; Shirude, P. S.; Hsu, S.-T. D.; Balasubramanian, S. Diarylethynyl Amides That Recognize the Parallel Conformation of Genomic Promoter DNA G-Quadruplexes. *J. Am. Chem. Soc.* **2008**, *130* (47), 15950−15956.

(14) Jain, A. K.; Reddy, V. V.; Paul, A.; Muniyappa, K.; Bhattacharya, S. Synthesis and Evaluation of a Novel Class of G-Quadruplex-Stabilizing Small Molecules Based on the 1,3-Phenylene-Bis(piperazinyl benzimidazole) System. *Biochemistry* **2009**, *48* (45), 10693−10704.

(15) Collie, G. W.; Sparapani, S.; Parkinson, G. N.; Neidle, S. Structural basis of telomeric RNA quadruplex−acridine ligand recognition. *J. Am. Chem. Soc.* **2011**, *133* (8), 2721−2728.

(16) Ginnari-Satriani, L.; Casagrande, V.; Bianco, A.; Ortaggi, G.; Franceschin, M. A hydrophilic three side-chained triazatruxene as a new strong and selective G-quadruplex ligand. *Org. Biomol. Chem.* **2009**, *7* (12), 2513−2516.

(17) Howorka, S.; Cheley, S.; Bayley, H. Sequence-specific detection of individual DNA strands using engineered nanopores. *Nat. Biotechnol.* **2001**, *19* (7), 636−639.

(18) An, N.; Fleming, A. M.; Burrows, C. J. Interactions of the Human Telomere Sequence with the Nanocavity of the α-Hemolysin Ion Channel Reveal Structure-Dependent Electrical Signatures for Hybrid Folds. *J. Am. Chem. Soc.* **2013**, *135* (23), 8562−8570.

(19) An, N.; Fleming, A. M.; Middleton, E. G.; Burrows, C. J. Single-molecule investigation of G-quadruplex folds of the human telomere sequence in a protein nanocavity. *Proc. Natl. Acad. Sci. U.S.A.* **2014**, *111* (40), 14325−14331.

(20) An, N.; Fleming, A. M.; White, H. S.; Burrows, C. J. Nanopore Detection of 8-Oxoguanine in the Human Telomere Repeat Sequence. *ACS Nano* **2015**, *9* (4), 4296−4307.

(21) Wanunu, M.; Dadosh, T.; Ray, V.; Jin, J.; McReynolds, L.; Drndić, M. Rapid electronic detection of probe-specific microRNAs using thin nanopore sensors. *Nat. Nanotechnol.* **2010**, *5* (11), 807−814.

(22) Wang, Y.; Zheng, D.; Tan, Q.; Wang, M. X.; Gu, L.-Q. Nanopore-based detection of circulating microRNAs in lung cancer patients. *Nat. Nanotechnol.* **2011**, *6* (10), 668−674.

(23) Lucas, F. L. R.; Versloot, R. C. A.; Yakovlieva, L.; Walvoort, M. T. C.; Maglia, G. Protein identification by nanopore peptide profiling. *Nat. Commun.* **2021**, *12* (1), 5795.

(24) Gu, L.-Q.; Braha, O.; Conlan, S.; Cheley, S.; Bayley, H. Stochastic sensing of organic analytes by a pore-forming protein containing a molecular adapter. *Nature* **1999**, *398* (6729), 686−690.

(25) Haque, F.; Lunn, J.; Fang, H.; Smithrud, D. B.; Guo, P. Real-time sensing and discrimination of single chemicals using the channel of phi29 DNA packaging nanomotor. *ACS Nano* **2012**, *6* (4), 3251−3261.

(26) Wu, H.-C.; Bayley, H. Single-Molecule Detection of Nitrogen Mustards by Covalent Reaction within a Protein Nanopore. *J. Am. Chem. Soc.* **2008**, *130* (21), 6813−6819.

(27) Kawano, R.; Osaki, T.; Sasaki, H.; Takinoue, M.; Yoshizawa, S.; Takeuchi, S. Rapid Detection of a Cocaine-Binding Aptamer Using Biological Nanopores on a Chip. *J. Am. Chem. Soc.* **2011**, *133* (22), 8474−8477.

(28) Faller, M.; Niederweis, M.; Schulz, G. E. The Structure of a Mycobacterial Outer-Membrane Channel. *Science* **2004**, *303* (5661), 1189−1192.

(29) Feng, Y.; Zhang, Y.; Ying, C.; Wang, D.; Du, C. Nanopore-based Fourth-generation DNA Sequencing Technology. *Genom. Proteom. Bioinform.* **2015**, *13* (1), 4−16.

(30) Ding, Y.; Fleming, A. M.; Burrows, C. J. α-Hemolysin nanopore studies reveal strong interactions between biogenic polyamines and DNA hairpins. *Microchim. Acta* **2016**, *183* (3), 973−979.

(31) Willems, K.; Van Meervelt, V.; Wloka, C.; Maglia, G. Single-molecule nanopore enzymology. *Philos. Trans. R. Soc., B* **2017**, *372* (1726), No. 20160230.

(32) Shi, W.; Friedman, A. K.; Baker, L. A. Nanopore Sensing. *Anal. Chem.* **2017**, *89* (1), 157−188.

(33) Heinz, C.; Engelhardt, H.; Niederweis, M. The Core of the Tetrameric Mycobacterial Porin MspA Is an Extremely Stable β-Sheet Domain. *J. Biol. Chem.* **2003**, *278*, 8678−8685.

(34) Loose, M.; Malla, S.; Stout, M. Real-time selective sequencing using nanopore technology. *Nat. Methods* **2016**, *13* (9), 751−754.

(35) Chingarande, R. G.; Tian, K.; Kuang, Y.; Sarangee, A.; Hou, C.; Ma, E.; Ren, J.; Hawkins, S.; Kim, J.; Adelstein, R.; et al. Real-time label-free detection of dynamic aptamer−small molecule interactions using a nanopore nucleic acid conformational sensor. *Proc. Natl. Acad. Sci. U. S. A.* **2023**, *120* (24), No. e2108118120.

(36) Butler, T. Z.; Pavlenok, M.; Derrington, I. M.; Niederweis, M.; Gundlach, J. H. Single-molecule DNA detection with an engineered MspA protein nanopore. *Proc. Natl. Acad. Sci. U.S.A.* **2008**, *105* (52), 20647−20652.

(37) Henley, R. Y.; Ashcroft, B. A.; Farrell, I.; Cooperman, B. S.; Lindsay, S. M.; Wanunu, M. Electrophoretic Deformation of Individual Transfer RNA Molecules Reveals Their Identity. *Nano Lett.* **2016**, *16* (1), 138−144.

(38) Riccardi, C.; Musumeci, D.; Russo Krauss, I.; Piccolo, M.; Irace, C.; Paduano, L.; Montesarchio, D. Exploring the conformational behaviour and aggregation properties of lipid-conjugated AS1411 aptamers. *Int. J. Biol. Macromol.* **2018**, *118*, 1384−1399.

https://doi.org/10.1021/acsami.4c19806
ACS Appl. Mater. Interfaces XXXX, XXX, XXX−XXX

(39) Ducani, C.; Bernardinelli, G.; Högberg, B.; Keppler, B. K.; Terenzi, A. Interplay of Three G-Quadruplex Units in the KIT Promoter. *J. Am. Chem. Soc.* **2019**, *141* (26), 10205−10213.
(40) Abraham, M. J.; Murtola, T.; Schulz, R.; Páll, S.; Smith, J. C.; Hess, B.; Lindahl, E. GROMACS: High performance molecular simulations through multi-level parallelism from laptops to supercomputers. *SoftwareX* **2015**, *1*−*2*, 19−25.
(41) Jorgensen, W. L.; Chandrasekhar, J.; Madura, J. D.; Impey, R. W.; Klein, M. L. Comparison of simple potential functions for simulating liquid water. *J. Chem. Phys.* **1983**, *79* (2), 926−935.
(42) Huang, J.; Rauscher, S.; Nawrocki, G.; Ran, T.; Feig, M.; De Groot, B. L.; Grubmüller, H.; MacKerell, A. D., Jr. CHARMM36m: an improved force field for folded and intrinsically disordered proteins. *Nat. Methods* **2017**, *14* (1), 71−73.
(43) Jo, S.; Kim, T.; Iyer, V. G.; Im, W. CHARMM-GUI: a web-based graphical user interface for CHARMM. *J. Comput. Chem.* **2008**, *29* (11), 1859−1865.
(44) Martínez, L.; Andrade, R.; Birgin, E. G.; Martínez, J. M. PACKMOL: A package for building initial configurations for molecular dynamics simulations. *J. Comput. Chem.* **2009**, *30* (13), 2157−2164.
(45) Mahfoud, M.; Sukumaran, S.; Hülsmann, P.; Grieger, K.; Niederweis, M. Topology of the porin MspA in the outer membrane of Mycobacterium smegmatis. *J. Biol. Chem.* **2006**, *281* (9), 5908−5915.
(46) Wang, Y.; Guan, X.; Zhang, S.; Liu, Y.; Wang, S.; Fan, P.; Du, X.; Yan, S.; Zhang, P.; Chen, H.-Y.; et al. Structural-profiling of low molecular weight RNAs by nanopore trapping/translocation using Mycobacterium smegmatis porin A. *Nat. Commun.* **2021**, *12* (1), 3368.
(47) Darden, T.; York, D.; Pedersen, L. Particle mesh Ewald: An *N*·log (*N*) method for Ewald sums in large systems. *J. Chem. Phys.* **1993**, *98* (12), 10089−10092.
(48) Hess, B.; Bekker, H.; Berendsen, H. J.; Fraaije, J. G. E. M. LINCS: a linear constraint solver for molecular simulations. *J. Comput. Chem.* **1997**, *18* (12), 1463−1472.
(49) Berendsen, H. J.; Postma, J. v.; Van Gunsteren, W. F.; DiNola, A.; Haak, J. R. Molecular dynamics with coupling to an external bath. *J. Chem. Phys.* **1984**, *81* (8), 3684−3690.
(50) Aksimentiev, A. J. N. Deciphering ionic current signatures of DNA transport through a nanopore. *Nanoscale* **2010**, *2* (4), 468−483.
(51) Tarek, M. Membrane electroporation: a molecular dynamics simulation. *Biophys. J.* **2005**, *88* (6), 4045−4053.
(52) Plesa, C.; van Loo, N.; Dekker, C. DNA nanopore translocation in glutamate solutions. *Nanoscale* **2015**, *7* (32), 13605−13609.
(53) Cao, J.; Zhang, S.; Zhang, J.; Wang, S.; Jia, W.; Yan, S.; Wang, Y.; Zhang, P.; Chen, H.-Y.; Huang, S. A single-molecule observation of dichloroaurate (I) binding to an engineered mycobacterium smegmatis porin A (MspA) nanopore. *Anal. Chem.* **2021**, *93* (3), 1529−1536.
(54) Fleming, S. J.; Lu, B.; Golovchenko, J. A. Charge, diffusion, and current fluctuations of single-stranded DNA trapped in an MspA nanopore. *Biophys. J.* **2017**, *112* (2), 368−375.
(55) Karsisiotis, A. I.; Hessari, N. M.; Novellino, E.; Spada, G. P.; Randazzo, A.; da Silva, M. W. Topological characterization of nucleic acid G-quadruplexes by UV absorption and circular dichroism. *Angew. Chem., Int. Ed. Engl.* **2011**, *123* (123), 10833−10836.
(56) Randazzo, A.; Spada, G. P.; da Silva, M. W. Circular Dichroism of Quadruplex Structures. In *Quadruplex Nucleic Acids*; Chaires, J. B., Graves, D., Eds.; Topics in Current Chemistry, 2012; Vol. *330*; Springer: Berlin, Heidelberg,; pp 67−86. DOI: .
(57) Ji, N.; Shi, H.-Q.; Fang, X.-Y.; Wu, Z.-Y. Exploring the interaction of G-quadruplex and porphyrin derivative by single protein nanopore sensing interface. *Anal. Chim. Acta* **2020**, *1106*, 126−132.
(58) Tian, K.; He, Z.; Wang, Y.; Chen, S.-J.; Gu, L.-Q. Designing a polycationic probe for simultaneous enrichment and detection of microRNAs in a nanopore. *ACS Nano* **2013**, *7* (5), 3962−3969.
(59) Sauer-Budge, A. F.; Nyamwanda, J. A.; Lubensky, D. K.; Branton, D. Unzipping kinetics of double-stranded DNA in a nanopore. *Phys. Rev. Lett.* **2003**, *90* (23), No. 238101.
(60) Wang, Y.; Tian, K.; Hunter, L. L.; Ritzo, B.; Gu, L.-Q. Probing molecular pathways for DNA orientational trapping, unzipping and translocation in nanopores by using a tunable overhang sensor. *Nanoscale* **2014**, *6* (19), 11372−11379.
(61) Perera, R. T.; Fleming, A. M.; Johnson, R. P.; Burrows, C. J.; White, H. S. Detection of benzo [a] pyrene-guanine adducts in single-stranded DNA using the α-hemolysin nanopore. *Nanotechnology* **2015**, *26* (7), No. 074002.
(62) Mereuta, L.; Asandei, A.; Dragomir, I.; Park, J.; Park, Y.; Luchian, T. A nanopore sensor for multiplexed detection of short polynucleotides based on length-variable, poly-arginine-conjugated peptide nucleic acids. *Anal. Chem.* **2022**, *94* (24), 8774−8782.
(63) Mathé, J.; Aksimentiev, A.; Nelson, D. R.; Schulten, K.; Meller, A. Orientation discrimination of single-stranded DNA inside the α-hemolysin membrane channel. *Proc. Natl. Acad. Sci. U. S. A.* **2005**, *102* (35), 12377−12382.
(64) Butler, T. Z.; Gundlach, J. H.; Troll, M. A. Determination of RNA orientation during translocation through a biological nanopore. *Biophys. J.* **2006**, *90* (1), 190−199.
(65) An, N.; Fleming, A. M.; White, H. S.; Burrows, C. J. Crown ether−electrolyte interactions permit nanopore detection of individual DNA abasic sites in single molecules. *Proc. Natl. Acad. Sci. U.S.A.* **2012**, *109* (29), 11504−11509.
(66) Butler, T. Z.; Gundlach, J. H.; Troll, M. Ionic current blockades from DNA and RNA molecules in the α-hemolysin nanopore. *Biophys. J.* **2007**, *93* (9), 3229−3240.
(67) Ciuca, A.; Asandei, A.; Schiopu, I.; Apetrei, A.; Mereuta, L.; Seo, C. H.; Park, Y.; Luchian, T. Single-molecule, real-time dissecting of peptide nucleic acid−DNA duplexes with a protein nanopore tweezer. *Anal. Chem.* **2018**, *90* (12), 7682−7690.

https://doi.org/10.1021/acsami.4c19806
ACS Appl. Mater. Interfaces XXXX, XXX, XXX−XXX